The electronic realization of synchronous machines: model matching, angle tracking and energy shaping techniques

Originally published in:
IEEE Transactions on Power Electronics 35(4), https://doi.org/10.1109/TPEL.2019.2939710

Funding acknowledgement:
160573 - Plug-and-Play Control & Optimization in Microgrids (SNF)

The electronic realization of synchronous machines: model matching, angle tracking and energy shaping techniques

Catalin Arghir and Florian Dörfler

***Abstract*—In this paper, we investigate grid-following and grid-forming control strategies starting from the nonlinear dynamics of the DC/AC converter. An electronic synchronous machine is an inverter whose the integral of the DC-bus measurement generates the angle of the instantaneous modulation vector. We show how this minimal augmentation represents an exact physical realization without requiring inner current loops. The DC-link capacitance becomes the equivalent rotational inertia of the converter. Additional features such as a novel phase-locked-loop design, a voltage controller and a power set-point tracking mechanism are then designed via two energy-shaping techniques. One energy function is used to implement a grid-following control scheme, via the inherent synchronizing torque, while the other is used to implement a grid-forming control scheme, by uncovering active-power droop. The results are first derived systematically, and then evaluated experimentally on a front-to-front setup.**

***Index Terms*—grid-forming, grid-following, converter control, angle synchronization, electronic synchronous machine**

I. Introduction

THE fundamental frequency is widely regarded as an indicator for power imbalance in machine-dominated grids. We develop a framework showing how the DC-bus measurement can complement that basis in future power grids.

In three-phase systems, energy typically flows through several conversion stages, such as a magnetic air-gaps or switching devices, circulates in passive circuits and is bound to satisfy certain requirements. Most energy conversion aspects [1], such as the modulation of power from one to two dimensions (i.e., from DC to AC) and the stabilization of the required harmonic motion, are addressed by VSCs operating in grid-forming or grid-following mode [2]. The typical VSC controllers employ inner loops which perform high-gain regulation of the quantities of interest from the input source to the point of power injection [3]. The power balance is achieved via multiple time-scales running in the feedback path, which settle at the appropriate steady-state. However, the large number of states of the inner loops makes the analysis of multiple converters difficult [4], motivating the study of more direct control approaches such as [5], [6].

With the growing complexity of the power system at large [7], the cascaded control structure can give rise to poorly understood interactions, causing phase-locked-loop (PLL) instabilities and oscillations of various kinds [8]. Towards the goal of improving overall system stability, virtual synchronous machines (VSMs) of various degrees of fidelity [9]–[11], are further implemented to emulate inertia and damping features. The VSM controller assigns set-points to the existing inner loops so that the currents and voltages behave according to a numerical model, while disregarding DC-link of the converter. In an increasingly underdamped converter landscape, impedance-based techniques [12], [13] explore the effects of PLLs, while comparative studies [4], [14], [15] show post-fault shortcomings of the conventional, small-signal approach.

In the mean time, control-theoretic advances brought more and more physical elements in the feedback design [16], [17], allowing modelling, control and stability analysis to be performed systematically. These methods, focused on stabilization of (networked) electro-mechanical systems, can provide insightful solutions for many complex problems arising in power conversion, and allow robust regulation without requiring inner loops, while providing guarantees on the quantities of interest. In this aim, we combine two fundamental control approaches: that of passivity-based control [16], centered on energy minimization, and that of output regulation [18], involving the internal model principle.

In this manuscript, we start from the paradigm first reported in [19], [20], and propose a rigorous, time-domain treatment of the factors leading to physical, as opposed to numerical, synchronous machine (SM) emulation. We show to what extent the machine dynamics are matched, via a coordinate transformation between the SM and the VSC state-space models. In an independent and parallel study [21], [22], we highlight the analogy between the electromotive force and air-gap torque of the SM, and the equivalent quantities of the inverter. Furthermore, we consider the reactive component of the air-gap torque, constituting the inherent SM synchronization mechanism, and construct an alternative for the PLL. We also show how active-power droop naturally emerges as a synchronizing torque by minimizing an energy function. In this way, we provide a unifying framework for control and stability analysis of grid-forming and grid-following behavior.

In contrast to similar studies [23]–[25], our work illustrates several ways in which large-signal synchronization can occur. An outcome of our design is a direct angle control scheme, similar in complexity to direct power control (DPC) [26], [27], which omits inner current loops and offers fast control of active and reactive power. In our case, the power set-

Manuscript submitted on March 12, 2019. This work was supported by the ETH Zürich funds and the SNF Assistant Professor Energy Grant #160573.

C. Arghir and F. Dörfler are with the Automatic Control Laboratory, ETH Zürich, 8092 Zürich, Switzerland. Emails: carghir@control.ee.ethz.ch, dorfler@ethz.ch.

point is achieved by appropriately controlling the converter angle, while still allowing a current controller to work in parallel rather than in cascade. This distinctive feature is the result of replacing reference tracking by a less restrictive nonlinear control design, related to geometric path following [17]. Finally, this work provides a control design method, a stability certification, and an experimental validation.

The rest of this paper is organised as follows: notation is introduced then, in Section II, the structural equivalence is presented. Section III offers a solution to the single-machine-infinite-bus problem used for grid-following, while Section IV presents a grid-forming design. Before concluding, Section V provides experimental results from a small-scale micro-grid.

A. Preliminaries and notation

We consider a three-phase, two-level active bridge driven by Pulse Width Modulation (PWM) with complementary duty-cycle ratios given as $d_{\mathrm{a}}(t)$, $d_{\mathrm{b}}(t)$ and $d_{\mathrm{c}}(t)$, each taking values from 0 to 1 during a switching cycle. By denoting the column vector $\boldsymbol{d}_{\mathrm{abc}} = [d_{\mathrm{a}}, d_{\mathrm{b}}, d_{\mathrm{c}}]$, we shall only focus on the continuous-time average-switch behavior and disregard the switching-frequency harmonics. Furthermore, by adopting Space Vector Modulation (SVM) terminology, we define the instantaneous modulation vector as

$$\boldsymbol{m}_{\mathrm{abc}}(t) = \boldsymbol{d}_{\mathrm{abc}}(t) - [\tfrac{1}{2}, \tfrac{1}{2}, \tfrac{1}{2}]\,. \tag{1}$$

We write this modulation vector in *machine orientation*, via its polar representation relative to the stationary frame as

$$\boldsymbol{m}_{\mathrm{abc}}(t) = m(t) \begin{bmatrix} -\sin(\theta(t)) \\ -\sin\left(\theta(t) - \frac{2\pi}{3}\right) \\ -\sin\left(\theta(t) + \frac{2\pi}{3}\right) \end{bmatrix}, \tag{2}$$

where $m(t) \in [0, \frac{1}{2}]$ and $\theta(t) \in [-\pi, \pi)$ are the instantaneous SVM magnitude and angle. We consider the *power-invariant* $\alpha\beta$-transformation and omit the zero sequence. Accordingly, $\boldsymbol{m}_{\alpha\beta}(t) = \sqrt{\frac{2}{3}} \begin{bmatrix} 1 & -\frac{1}{2} & -\frac{1}{2} \\ 0 & \frac{\sqrt{3}}{2} & -\frac{\sqrt{3}}{2} \end{bmatrix} \boldsymbol{m}_{\mathrm{abc}}(t)$ is defined so that

$$\boldsymbol{m}_{\alpha\beta}(t) = \mu(t) \begin{bmatrix} -\sin\theta(t) \\ \cos\theta(t) \end{bmatrix}, \tag{3}$$

where $\mu(t) = \sqrt{3/2} m(t)$ denotes the modulation magnitude in this $\alpha\beta$-frame. Furthermore, we write the identity matrix as $\mathbf{I} = \left[\begin{smallmatrix} 1 & 0 \\ 0 & 1 \end{smallmatrix}\right]$ and the rotation matrix as $\mathbf{R}_\phi = \begin{bmatrix} \cos\phi & -\sin\phi \\ \sin\phi & \cos\phi \end{bmatrix}$. Given a two dimensional vector $\boldsymbol{x} = \left[\begin{smallmatrix} x_1 \\ x_2 \end{smallmatrix}\right]$, we define its magnitude as $\|\boldsymbol{x}\| = \sqrt{x_1^2 + x_2^2}$. We shall also make use of the partial differential operator $\frac{\partial}{\partial x} = \nabla$ when x is a scalar (will always be an angle variable), and $\frac{\partial}{\partial \boldsymbol{x}} = \begin{bmatrix} \frac{\partial}{\partial x_1} & \frac{\partial}{\partial x_2} \end{bmatrix}$ as a row vector when $\boldsymbol{x}$ is a two-dimensional column vector.

II. The inverter-machine equivalence

To study the fundamental energy modulation mechanism of inverters and electrical machines alike, we adopt a stationary frame and identify the structural equivalence between the two.

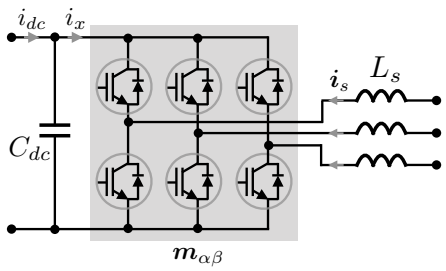

Fig. 1. The inverter depicted with its DC-link capacitor and switched inductor.

A. The VSC model

Considering the DC-supply current i_{dc} and the AC-grid voltage $\boldsymbol{v}_g$ as external inputs, we model the VSC

$$C_{dc} \frac{\mathrm{d}u_{dc}}{\mathrm{d}t} = -G_{dc} u_{dc} + i_{dc} + \boldsymbol{m}_{\alpha\beta}^\top \boldsymbol{i}_s \tag{4a}$$

$$L_s \frac{\mathrm{d}\boldsymbol{i}_s}{\mathrm{d}t} = -R_s \boldsymbol{i}_s + \boldsymbol{v}_g - \boldsymbol{m}_{\alpha\beta} u_{dc}\,, \tag{4b}$$

in $\alpha\beta$-frame, where, apart from the elements in Fig. 1, G_{dc} is a parallel conductance modeling (switching) losses in the DC-link, while R_s models the (conduction) losses in series with the switching inductor.

We consider the main nonlinearity to be the power-preserving structure depicted in Fig. 2, where the average-switch current drawn from the DC-link is denoted by i_x, while the AC-side average-switch voltage is denoted by $\boldsymbol{e}_x$. These quantities will be related to the SM air-gap torque and, respectively, the electromotive force (EMF).

$$i_x = -\boldsymbol{m}_{\alpha\beta}^\top \boldsymbol{i}_s \quad \Leftrightarrow \quad \boldsymbol{e}_x = \boldsymbol{m}_{\alpha\beta} u_{dc}$$

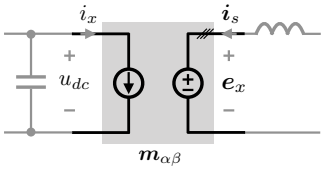

Fig. 2. The core element of an inverter: the DC-AC energy transformation mechanism, satisfying power balance $u_{dc} i_x + \boldsymbol{e}_x^\top \boldsymbol{i}_s = 0$, and modulated by the two dimensional signal $\boldsymbol{m}_{\alpha\beta}$.

Note that the signal $\boldsymbol{m}_{\alpha\beta}$, regardless of the control law, cannot inject or extract energy into the system: it acts in a lossless manner. To see this, we define the storage function

$$\mathcal{H} = \tfrac{1}{2} C_{dc} u_{dc}^2 + \tfrac{1}{2} \boldsymbol{i}_s^\top L_s \boldsymbol{i}_s\,, \tag{5}$$

and observe that the change in total energy occurring during any evolution of system (4) does not depend on $\boldsymbol{m}_{\alpha\beta}$

$$\begin{aligned} \frac{\mathrm{d}\mathcal{H}}{\mathrm{d}t} &= C_{dc} u_{dc} \frac{\mathrm{d}u_{dc}}{\mathrm{d}t} + \boldsymbol{i}_s^\top L_s \frac{\mathrm{d}\boldsymbol{i}_s}{\mathrm{d}t} \\ &= \underbrace{-G_{dc} u_{dc}^2 - \boldsymbol{i}_s^\top R_s \boldsymbol{i}_s}_{\text{internal dissipation}} + \underbrace{i_{dc} u_{dc} + \boldsymbol{i}_s^\top \boldsymbol{v}_g}_{\text{external injection}}\,. \end{aligned} \tag{6}$$

As we shall see, the role of $\boldsymbol{m}_{\alpha\beta}$ is to streamline the flow from the DC-side into the grid, an energy transfer property.

B. The SM model

Consider the model of a SM having constant rotor excitation, whose derivation is presented in Appendix A:

$$\frac{\mathrm{d}\theta}{\mathrm{d}t} = \omega \tag{7a}$$

$$M\frac{\mathrm{d}\omega}{\mathrm{d}t} = -D\omega + \tau_m + L_m i_r^* \left[\begin{smallmatrix} -\sin\theta \\ \cos\theta \end{smallmatrix}\right]^\top \boldsymbol{i}_s \tag{7b}$$

$$L_s\frac{\mathrm{d}\boldsymbol{i}_s}{\mathrm{d}t} = -R_s\boldsymbol{i}_s + \boldsymbol{v}_g - L_m i_r^* \left[\begin{smallmatrix} -\sin\theta \\ \cos\theta \end{smallmatrix}\right]\omega\,. \tag{7c}$$

The energy transfer now occurs in the machine air-gap, modulated by the excitation current i_r^*, as illustrated in Fig. 3

$$\tau_e = -L_m i_r^* \left[\begin{smallmatrix} -\sin\theta \\ \cos\theta \end{smallmatrix}\right]^\top \boldsymbol{i}_s \tag{8a}$$

$$\boldsymbol{e}_s = L_m i_r^* \left[\begin{smallmatrix} -\sin\theta \\ \cos\theta \end{smallmatrix}\right]\omega\,. \tag{8b}$$

In a conventional PLL design [28], as well as in some simplified SM models [4], the electrical torque (8a) is represented by $\sin(\theta-\theta_g)$, where θ_g is the angle of the grid voltage. This is what we later call the synchronizing torque since, upon closer inspection, it appears as an energy minimization term, motivating our study in the remainder of this paper.

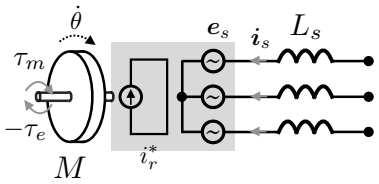

Fig. 3. The SM with constant excitation, satisfying the lossless energy transfer property $\omega\tau_e + \boldsymbol{e}_s^\top \boldsymbol{i}_s = 0$, and modulated by the one dimensional signal i_r^*.

The matching control presented next is designed to synthesize all elements of the SM model (7) using corresponding elements of the inverter model (4), upon augmenting an integrator in the closed loop. As illustrated in (6), due to its energy-conservation property, $\boldsymbol{m}_{\alpha\beta}$ cannot be used to implement a lossy element, such as a damper winding. This is why we restrict ourselves to matching the ideal SM with constant excitation current.

C. The electronic synchronous machine

We start by denoting ω_0 as the nominal angular velocity, corresponding to the grid frequency, and u_{dc}^* as the reference DC-link voltage, related to the grid voltage level. Consider system (4), for which we use the modulation (3) to identify a similar energy-conversion structure as in the SM

$$i_x = -\mu \left[\begin{smallmatrix} -\sin\theta \\ \cos\theta \end{smallmatrix}\right]^\top \boldsymbol{i}_s \tag{9a}$$

$$\boldsymbol{e}_x = \mu \left[\begin{smallmatrix} -\sin\theta \\ \cos\theta \end{smallmatrix}\right] u_{dc}\,. \tag{9b}$$

This key analogy prompts us to augment (4) with an integrator for the DC-link voltage in the same way that, in the mechanical domain, the rotor angle integrates the angular velocity (11a)

$$\frac{\mathrm{d}\theta}{\mathrm{d}t} = \eta u_{dc}\,. \tag{10}$$

By choosing the scaling factor $\eta = \omega_0/u_{dc}^*$, we define the equivalent angular velocity of the inverter as $\omega = \eta u_{dc}$. Here, η converts units of voltage into units of angular velocity, but also units of torque into units of current. This coordinate transformation allows us to select the constant modulation magnitude $\mu = \eta L_m i_r^*$ in (3) and complete the exact model-matching design by identifying $i_x/\eta = \tau_e$ and $\boldsymbol{e}_x = \boldsymbol{e}_s$ with the SM air-gap torque and EMF (8), respectively.

We are now able to rewrite, via $\omega = \eta u_{dc}$, the closed-loop system (10), (4), (3), referred to as the *electronic SM* (eSM)

$$\frac{\mathrm{d}\theta}{\mathrm{d}t} = \omega \tag{11a}$$

$$\frac{C_{dc}}{\eta^2}\frac{\mathrm{d}\omega}{\mathrm{d}t} = -\frac{G_{dc}}{\eta^2}\omega + \frac{i_{dc}}{\eta} + \frac{\mu}{\eta}\left[\begin{smallmatrix} -\sin\theta \\ \cos\theta \end{smallmatrix}\right]^\top \boldsymbol{i}_s \tag{11b}$$

$$L_s\frac{\mathrm{d}\boldsymbol{i}_s}{\mathrm{d}t} = -R_s\boldsymbol{i}_s + \boldsymbol{v}_g - \frac{\mu}{\eta}\left[\begin{smallmatrix} -\sin\theta \\ \cos\theta \end{smallmatrix}\right]\omega\,. \tag{11c}$$

By comparing (11) to (7), we further identify the equivalent mechanical torque $i_{dc}/\eta = \tau_m$, rotor moment of inertia $C_{dc}/\eta^2 = M$ and rotor damping coefficient $G_{dc}/\eta^2 = D$. Consequently, the inertia introduced by this model-matching control corresponds to instantaneous physical energy stored in the DC-link. Moreover, the magnetisation factor appears as $\mu/\eta = L_m i_r^*$, while the stator self-inductance L_s of the SM is identified with the switching-side inductance of the inverter.

As a general guideline, to achieve a nominal EMF voltage amplitude $\|\boldsymbol{e}_s\| = e_0$, the rotor excitation can be chosen as $i_r^* = e_0/(\omega_0 L_m)$, from which we can determine $\mu = e_0/u_{dc}^*$. As we shall see in the rest of this paper, the value of μ can be adjusted to achieve additional objectives for the eSM.

D. Inertia and damping augmentation

Compared to rotating machinery, the power-electronics sourced DC-current i_{dc} has a much faster actuation bandwidth than the valve of a turbine governor. This DC input can implement, for instance, a standard proportional-integral-derivative (PID) control of the form

$$i_{dc} = -K_p(u_{dc} - u_{dc}^*) - K_i x_{dc} - K_d\frac{\mathrm{d}u_{dc}}{\mathrm{d}t} \tag{12a}$$

$$\frac{\mathrm{d}x_{dc}}{\mathrm{d}t} = u_{dc} - u_{dc}^*\,, \tag{12b}$$

where x_{dc} is the state of the integrator. The gains K_p and K_d add extra damping and inertia to the terms G_{dc} and, respectively, C_{dc} in (11), contributing physically to the energy balance. In the following sections, we will replace the conventional integral term with an explicit pre-computation of the steady-state bias.

E. Frequency behavior of the eSM

The eSM enables the coupling between AC frequency and DC voltage, allowing the inverter to function without a conventional phase-locked loop (PLL) and in both stiff and weak grids, such as in Fig. 4. Broadly speaking, in a stiff grid the internal eSM frequency adapts to an external frequency by charging or discharging its DC-link voltage. Alternatively, if the grid does not impose a certain frequency, the DC-link maintains its nominal value, and the eSM forms the system frequency. Thus, adopting the grid-following or grid-forming classifications, the eSM can function in either mode.

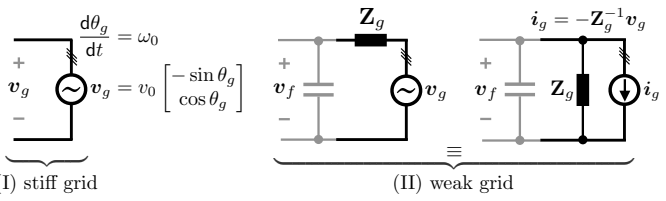

Fig. 4. The two types of AC-busses considered: (I) a stiff voltage source and (II) a local AC-capacitor charged by a distant source and its Norton equivalent. Throughout this paper $\boldsymbol{v}_g$ and $\boldsymbol{i}_g$ will be sinusoidal of constant amplitude and constant frequency ω_0.

In the following sections, we make these ideas precise and study the large-signal behavior. We first treat the stiff and weak grid cases separately, discussing two ways in which synchronization naturally emerges. Finally, we combine the two in an experiment where the frequency is not driven by an external source.

III. Synchronization to a Stiff Grid

Our goal now is to determine the current injection i_{dc} which, in conjunction with the matching modulation $\boldsymbol{m}_{\alpha\beta}$, achieves three basic control objectives: (*i*) DC-bus regulation, (*ii*) angle synchronization and (*iii*) internal stability. Although there are situations in which the DC-current is not available as a control input, but rather acts as a disturbance, our framework is general enough to provide an informative solution.

Consider the inverter connected to a stiff AC-voltage bus given by a sinusoidal signal of constant amplitude v_0 and constant frequency ω_0, as in Fig. 5. The power flow is directly reflected in the relationship between the internal voltage vector $\boldsymbol{e}_x$ and the grid voltage $\boldsymbol{v}_g$, seen at the terminals of the eSM. To control the angle difference between these two vectors, we construct an energy function whose minimization is performed by the inherent eSM synchronizing torque.

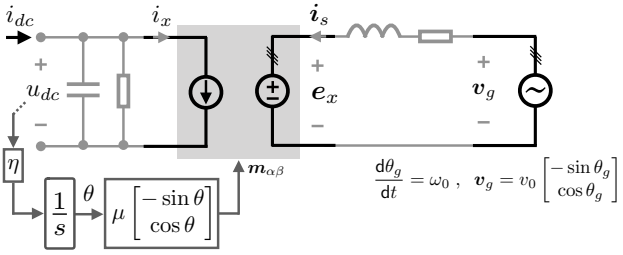

Fig. 5. Equivalent circuit of the eSM (11) connected to a stiff grid.

A. The eSM synchronizing torque

Observe that, when the DC-bus is firmly regulated, namely when $u_{dc} = u_{dc}^*$, the switching-node voltage $\boldsymbol{e}_x$ becomes sinusoidal, of constant amplitude μu_{dc}^* and frequency ηu_{dc}^* which, for a steady-state solution to exist, must be equal to ω_0. In this case the inductor current (4b) attains a sinusoidal solution as $t \to \infty$. Thus, we say that the stiff angle dynamics (both θ and θ_g) are dominant[1] and induce a *steady-state response*. In accordance with the internal model principle [29], we express this as the angle-dependent solution

$$\hat{\boldsymbol{i}}_s = \mathbf{Z}_s^{-1}\big(\boldsymbol{v}_g - \mu u_{dc}^* \begin{bmatrix} -\sin\theta \\ \cos\theta \end{bmatrix}\big), \tag{13}$$

where $\mathbf{Z}_s = \begin{bmatrix} R_s & -\omega_0 L_s \\ \omega_0 L_s & R_s \end{bmatrix}$, its inverse is $\mathbf{Z}_s^{-1} = \|\mathbf{Z}_s\|^{-2}\mathbf{Z}_s^\top$ and its matrix norm $\|\mathbf{Z}_s\| = \sqrt{R_s^2 + \omega_0^2 L_s^2}$. In general, when the DC-bus is in transient, (13) only represents a steady-state preview signal and serves as an analysis tool.

In order to maintain the DC-bus at steady-state, the upstream injection i_{dc} must adopt a suitable internal model, i.e. a feed-forward bias, which we can derive from the switching current

$$\begin{aligned} \hat{i}_x &= -\boldsymbol{m}_{\alpha\beta}^\top \hat{\boldsymbol{i}}_s \\ &= -\mu \begin{bmatrix} -\sin\theta \\ \cos\theta \end{bmatrix}^\top \mathbf{Z}_s^{-1}\big(\boldsymbol{v}_g - \mu u_{dc}^* \begin{bmatrix} -\sin\theta \\ \cos\theta \end{bmatrix}\big) \\ &= \underbrace{\tfrac{\mu v_0 R_s}{\|\mathbf{Z}_s\|^2}\big(\tfrac{\mu u_{dc}^*}{v_0} - \cos(\theta - \theta_g)\big)}_{(a)} + \underbrace{\tfrac{\mu v_0 \omega_0 L_s}{\|\mathbf{Z}_s\|^2}\sin(\theta - \theta_g)}_{(b)}. \end{aligned} \tag{14}$$

The relevance of this formulation is that it provides a guideline for angle synchronization. By commanding i_{dc} to account solely for term (a), corresponding to the active part of $\hat{i}_x$, the closed loop would only feature the reactive part (b). We call this the inherent synchronizing torque of the eSM.

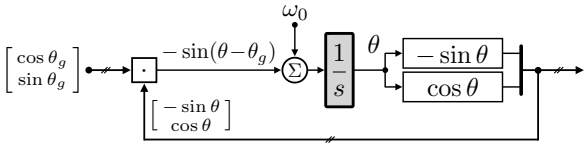

Fig. 6. The prototypical structure of a (unit-gain) PLL showing the synchronisation torque $-\sin(\theta - \theta_g)$. Here $\cdot$ denotes the vector dot product.

Observe that the term (b) can be also expressed as the gradient of a quadratic function. We call this the *synchronization potential*, anticipating the energy stored in the inductor. As it turns out, this energy function takes the form

$$\begin{aligned} \mathcal{S} &= \tfrac{1}{2}\hat{\boldsymbol{i}}_s^\top L_s \hat{\boldsymbol{i}}_s \\ &= \tfrac{1}{2}\tfrac{L_s}{\|\mathbf{Z}_s\|^2}\big(\mu^2 u_{dc}^{*2} - 2\mu u_{dc}^* v_0 \cos(\theta - \theta_g) + v_0^2\big). \end{aligned} \tag{15}$$

In essence, we aim to drive the angle difference $\theta_{dq} = \theta - \theta_g$ to a value which minimises the energy function $\mathcal{S}$, as seen in Fig. 7. While in this case the minimizer represents zero angle-difference, we will later provide a way to achieve a more general operating point.

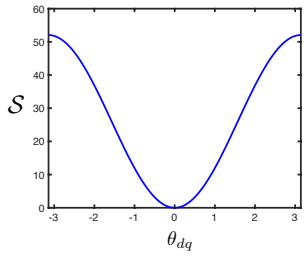

Fig. 7. A plot of the synchronization potential $\mathcal{S}$ as a function of $\theta_{dq} = \theta - \theta_g$, with minimum at 0 and maximum at $\pm\pi$.

The internal model variables, $\hat{\boldsymbol{i}}_s$ and $\hat{i}_x$, can be computed in real-time from the angle variables. They are also useful in constructing transient dynamics and stability certificates.

[1] i.e., lacking any form of dissipation, having the slowest decay rate

B. Error-coordinates analysis

We now pursue a systematic design procedure for the DC-side control law i_{dc} by formulating a stabilization problem for the error dynamics of the eSM system. Consider the grid-attached dq-frame $\theta_{dq} = \theta - \theta_g$ and $\boldsymbol{i}_{dq} = \mathbf{R}_{\theta_g}^\top \boldsymbol{i}_s$. In these coordinates, the internal model (13) becomes a function of the angle difference θ_{dq}. By defining $\hat{\boldsymbol{i}}_{dq}(\theta_{dq}) = \mathbf{R}_{\theta_g}^\top \hat{\boldsymbol{i}}_s$ and

$$\mathcal{S}(\theta_{dq}) = \tfrac{1}{2}\hat{\boldsymbol{i}}_{dq}(\theta_{dq})^\top L_s \hat{\boldsymbol{i}}_{dq}(\theta_{dq})\,, \tag{16}$$

we are able to express the control specifications in terms of driving the error system to zero as $t \to \infty$

(*i*) DC-bus regulation: $u_{dc} \to u_{dc}^*$;
(*ii*) angle synchronization[2]: $\theta_{dq} \to \theta_{dq}^*$ s.t. $\nabla\mathcal{S}(\theta_{dq}^*) = 0$;
(*iii*) internal stability: $\boldsymbol{i}_{dq} \to \hat{\boldsymbol{i}}_{dq}(\theta_{dq})$.

In essence, the energy-based control technique presented in Appendix B considers the dynamics of the error coordinates, as well as a shifted energy function derived from (5). This ultimately leads to the stabilizing control law

$$i_{dc} = \underbrace{-K_p(u_{dc} - u_{dc}^*)}_{\text{P-control}} + \underbrace{G_{dc}u_{dc}^* + \hat{i}_x(\theta_{dq})}_{\text{steady-state bias}} \underbrace{-\eta\nabla\mathcal{S}(\theta_{dq})}_{\text{synchronization}}\,, \tag{17}$$

by adding damping, matching the appropriate terms and, respectively, minimizing the potential energy. The task of producing this current is carried out by the upstream converter, typically a boost or an active rectifier. The proposed controller achieves objective (*iii*) indirectly: by stabilizing the DC-voltage, the appropriate steady-state is consequently induced.

From a physical point of view, the steady-state bias together with the synchronization term represent a feed-forward injection of the AC-side losses anticipated by the internal model

$$\hat{i}_x(\theta_{dq}) - \eta\nabla\mathcal{S}(\theta_{dq}) = \hat{\boldsymbol{i}}_s^\top R_s \hat{\boldsymbol{i}}_s\,, \tag{18}$$

and can be computed in stationary frame via (13). It actually performs the cancelation of the term (a). What remains in the closed loop is a transient term $i_x - \hat{i}_x$, which is dominated by damping, and the synchronizing torque

$$\eta\nabla\mathcal{S}(\theta_{dq}) = \tfrac{\mu v_0 \omega_0 L_s}{\|\mathbf{Z}_s\|^2}\sin\theta_{dq}\,, \tag{19}$$

corresponding to the term (b), the reactive part of $\hat{i}_x$.

To focus on the angle behavior, we neglect the inductor current transients, i.e. we assume that $\boldsymbol{i}_{dq} = \hat{\boldsymbol{i}}_{dq}(\theta_{dq})$, hence also $i_x = \hat{i}_x(\theta_{dq})$, for all time, and consider subsystem (11a), (11b) with input (17)

$$\frac{\mathrm{d}\theta_{dq}}{\mathrm{d}t} = \eta\tilde{u}_{dc} \tag{20a}$$

$$C_{dc}\frac{\mathrm{d}\tilde{u}_{dc}}{\mathrm{d}t} = -(G_{dc}+K_p)\tilde{u}_{dc} - \eta\nabla\mathcal{S}(\theta_{dq})\,, \tag{20b}$$

where $\tilde{u}_{dc} = u_{dc} - u_{dc}^*$. In this way, the eSM can be seen as analogous to a damped pendulum where the tangential component of gravity (corresponding to the gradient term) drives the mass to a rest position having zero angle with respect to the downward vertical axis (corresponding to the grid voltage vector here). This mechanical analogy, illustrated in Fig. 8, is also known as the swing equations, an important tool in studying synchronization in power networks [30].

This is also represented as block-diagram in Fig. 9. Alternatively, the proposed PLL can be seen as a second-order gradient descent, an algorithm which settles when the gradient vanishes. Among the configurations where $\nabla\mathcal{S}(\theta_{dq}) = 0$, the point of interest is the stable equilibrium $\theta_{dq} = 0$.

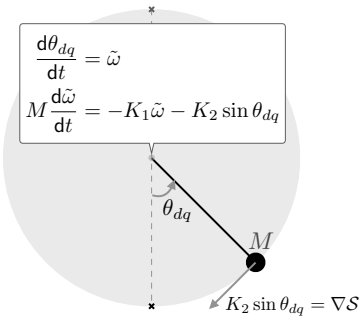

Fig. 8. The eSM system (11) in feedback with (17), when $\boldsymbol{i}_{dq} = \hat{\boldsymbol{i}}_{dq}$, shown in error coordinates $\tilde{\omega} = \eta\tilde{u}_{dc}$. Here, $M = C_{dc}/\eta^2$ and $K_1 = (C_{dc} + K_p)/\eta^2$ are related to the pendulum moment of inertia and damping.

To further account for inductor current transients, an energy-based stability analysis is pursued in Appendix B, by considering $\tilde{\boldsymbol{i}}_{dq} = \boldsymbol{i}_{dq} - \hat{\boldsymbol{i}}_{dq}(\theta_{dq})$, and the energy function

$$\tilde{\mathcal{H}}(\theta_{dq}, \tilde{u}_{dc}, \tilde{\boldsymbol{i}}_{dc}) = \tfrac{1}{2}C_{dc}\tilde{u}_{dc}^2 + \mathcal{S}(\theta_{dq}) + \tfrac{1}{2}\tilde{\boldsymbol{i}}_{dq}^\top L_s \tilde{\boldsymbol{i}}_{dq}\,. \tag{21}$$

This extends the nonlinear stability proof of the damped pendulum to the eSM with inductor dynamics, thus guaranteeing the control objectives. The analysis suggests that, in order to prevent full revolutions of the angle, sufficient (active) damping must be present on the DC-link.

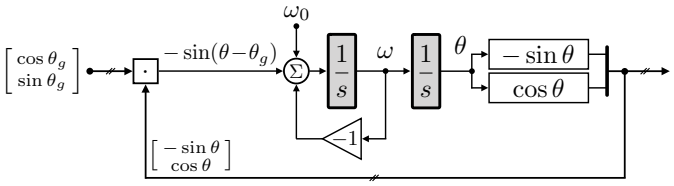

Fig. 9. The prototypical structure of a second-order PLL showing the synchronisation torque $-\sin(\theta - \theta_g)$, and the additional state variable ω, where $\omega \to \omega_0$ along with $\theta \to \theta_g$, as $t \to \infty$. Both the PLL gain and the time constant of ω are set to 1 for simplicity of exposition.

Remark 1 (Mode-switching feature) *From Fig. 9, we see that the primary distinction to conventional PLL design is that the state $\omega = \eta u_{dc}$ is represented by the* DC*-voltage of the inverter. By looking at* (19)*, we also notice that the gain of the synchronizing torque depends on the grid voltage magnitude, $\|\boldsymbol{v}_g\| = v_0$. When the grid is absent, this term vanishes and so the converter angle is driven solely by the* DC*-bus, which tracks the reference $u_{dc}^* = \omega_0/\eta$. In this way, the converter switches from grid-following to grid-forming mode.*

C. Direct angle control

There are scenarios in which the upstream converter cannot provide any further degree of freedom other than DC-bus

[2]throughout this paper, ∇ will always be taken w.r.t. the variable θ_{dq}

regulation. We can design an alternative, first-order angle synchronization mechanism, by replacing the controller defined by the pair (10), (17) with

$$\frac{\mathrm{d}\theta}{\mathrm{d}t} = \eta u_{dc} - \kappa' \nabla \mathcal{S} \tag{22a}$$

$$i_{dc} = -K_p(u_{dc} - u^*_{dc}) + G_{dc} u^*_{dc} + \hat{i}_x \,, \tag{22b}$$

where κ' plays the role of a PLL gain. When compared to (20), the transients are similar and settle at the same equilibrium. The main advantage is that, effectively, the gain κ' is implemented purely in software and is decoupled from the damping injection K_p, subject to the control bandwidth limitations of the upstream converter. In this case, the entire expression (22b) can be replaced by a conventional PID design. Finally, exact matching no longer occurs as the gradient term resembles the slip torque of an induction machine.

D. PQ set-point tracking

For simplicity of exposition we consider the L-filter case here. The proposed control structure (17) so far achieves zero angle difference between $\boldsymbol{e}_x$ and $\boldsymbol{v}_g$. This is due to the construction of the function $\mathcal{S}$, having its minimum at $\theta^*_{dq} = 0$. Building on top of that, we can design μ and modify the potential energy $\mathcal{S}$ to allow an arbitrary operating point. Let us define the instantaneous active and reactive powers, and their internal-model counterparts (also depending on θ_{dq}), as

$$\begin{aligned} P_g &= -\boldsymbol{i}_s^\top \boldsymbol{v}_g \\ Q_g &= -\boldsymbol{i}_s^\top \left[\begin{smallmatrix} 0 & 1 \\ -1 & 0 \end{smallmatrix}\right] \boldsymbol{v}_g \end{aligned} \quad \Bigg| \quad \begin{aligned} \hat{P}_g(\theta_{dq}) &= -\hat{\boldsymbol{i}}_s^\top \boldsymbol{v}_g \\ \hat{Q}_g(\theta_{dq}) &= -\hat{\boldsymbol{i}}_s^\top \left[\begin{smallmatrix} 0 & 1 \\ -1 & 0 \end{smallmatrix}\right] \boldsymbol{v}_g \,. \end{aligned} \tag{23}$$

Assuming we are given a set-point (P^*_g, Q^*_g), we aim to find the corresponding μ^* and θ^*_{dq} which further achieves power tracking as $t \to \infty$. The overall control objectives become:

(*i*) DC-bus regulation: $u_{dc} \to u^*_{dc}$;
(*ii*) PQ tracking: $\theta_{dq} \to \theta^*_{dq}$ s.t. $(\hat{P}_g, \hat{Q}_g)(\theta^*_{dq}) = (P^*_g, Q^*_g)$;
(*iii*) internal stability: $\boldsymbol{i}_{dq} \to \hat{\boldsymbol{i}}_{dq}(\theta_{dq})$.

Notice that, when all three objectives are satisfied, the modulation settles at a constant magnitude μ^* and an angle θ^* rotating with constant angular velocity ω_0, just like the grid angle. Since we can define $\theta^*_{dq} = \theta^* - \theta_g$, the inductor current producing the desired power injection $P^*_g = \hat{P}_g(\theta^*_{dq})$, $Q^*_g = \hat{Q}_g(\theta^*_{dq})$ corresponds to $\boldsymbol{i}^*_{dq} = \hat{\boldsymbol{i}}_{dq}(\theta^*_{dq})$. We are able to compute this quantity in $\alpha\beta$-frame as $\boldsymbol{i}^*_s = \mathbf{R}_{\theta_g} \boldsymbol{i}^*_{dq}$, via the grid measurement $\boldsymbol{v}_g = (v_{g_\alpha}, v_{g_\beta})$

$$\boldsymbol{i}^*_s = \frac{1}{\|\boldsymbol{v}_g\|^2} \begin{bmatrix} v_{g_\alpha} & v_{g_\beta} \\ -v_{g_\beta} & v_{g_\alpha} \end{bmatrix} \begin{bmatrix} P^*_g \\ Q^*_g \end{bmatrix}, \tag{24}$$

from which we extract the features of the modulation vector

$$\mu^* = \frac{1}{u^*_{dc}} \|\boldsymbol{v}_g - \mathbf{Z}_s \boldsymbol{i}^*_s\| \tag{25a}$$

$$\begin{bmatrix} -\sin\theta^* \\ \cos\theta^* \end{bmatrix} = \frac{1}{\mu^* u^*_{dc}} \left(\boldsymbol{v}_g - \mathbf{Z}_s \boldsymbol{i}^*_s\right). \tag{25b}$$

This calculation can also be seen in the block diagrams of Fig. 10. Finally, we use $\mu = \mu^*$ in $\boldsymbol{m}_{\alpha\beta}$ and, by replacing $\mathcal{S}(\theta_{dq})$ with $\mathcal{S}(\theta_{dq} - \theta^*_{dq})$, we modify controller (17) as below

$$i_{dc} = -K_p \tilde{u}_{dc} + G_{dc} u^*_{dc} + \hat{i}_x(\theta_{dq}) - \eta \nabla \mathcal{S}(\theta_{dq} - \theta^*_{dq}) \,. \tag{26}$$

The synchronization torque can be computed in $\alpha\beta$-frame

$$\begin{aligned} \nabla \mathcal{S}(\theta_{dq} - \theta^*_{dq}) &= \frac{\mu^* v_0 \omega_0 L_s}{\eta \|\mathbf{Z}_s\|^2} \begin{bmatrix} -\sin\theta \\ \cos\theta \end{bmatrix}^\top \begin{bmatrix} 0 & 1 \\ -1 & 0 \end{bmatrix} \begin{bmatrix} -\sin\theta^* \\ \cos\theta^* \end{bmatrix} \\ &= \frac{\mu^* v_0 \omega_0 L_s}{\eta \|\mathbf{Z}_s\|^2} \sin(\theta - \theta^*) \,. \end{aligned} \tag{27}$$

Due to the flexibility of direct angle control (22), the gain $\kappa = \kappa' \frac{\mu^* v_0 \omega_0 L_s}{\eta \|\mathbf{Z}_s\|^2}$ in Fig. 10 (bottom side) can be tuned via κ'.

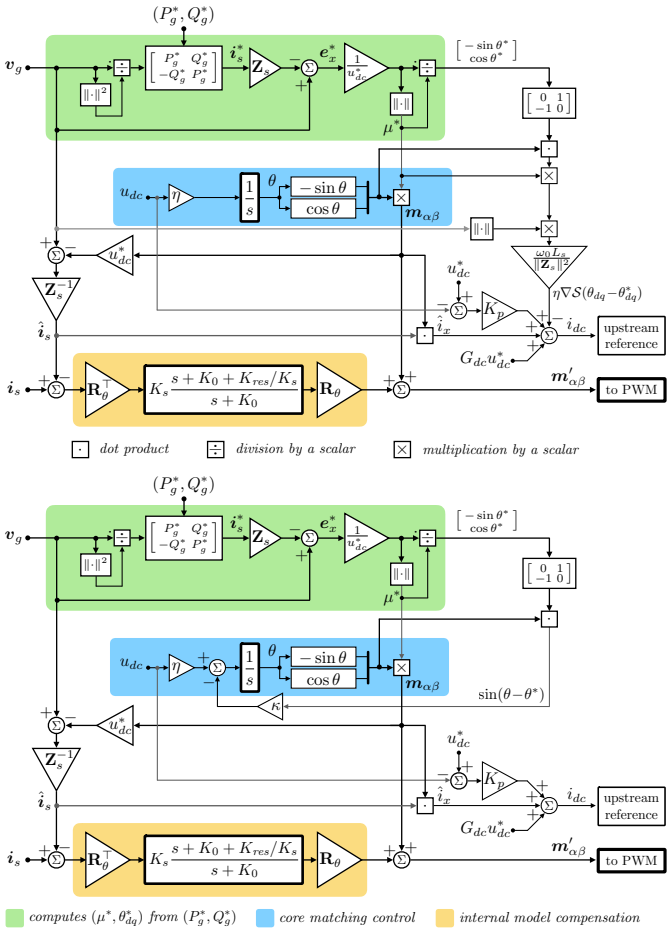

Fig. 10. Block diagrams of the two control structures implementing PQ set-point tracking, (10),(26)-top and (22)-bottom, augmented with internal model correction (28). Here, i_{dc} is given as a reference for the output current of the upstream converter and $\boldsymbol{m}'_{\alpha\beta}$ is the modulation signal sent to the PWM.

Since the DC-link voltage, the angle difference and the inductor current stabilize in the same manner as before, we have that all three objectives are attained simultaneously, without requiring the assumption of time-scale separation and without tracking $\boldsymbol{i}^*_s$ directly. The nonlinear stability analysis in Appendix B pertains when replacing $\mathcal{S}(\theta_{dq})$ with $\mathcal{S}(\theta_{dq} - \theta^*_{dq})$ in the Hamiltonian function (21).

E. Internal model correction

Due to model uncertainty in formulas such as (13), and later (31), the internal model representation can become inaccurate, resulting in a miss-aligned steady-state operation. One way to correct this is to actively pursue objective (*iii*). In this aim,

the modulation vector can be augmented with a proportional-resonant controller enforcing $\boldsymbol{i}_s \to \hat{\boldsymbol{i}}_s$ as $t \to \infty$:

$$\begin{aligned} \boldsymbol{m}'_{\alpha\beta} &= \mu^* \left[\begin{smallmatrix} -\sin\theta \\ \cos\theta \end{smallmatrix}\right] + K_s(\boldsymbol{i}_s - \hat{\boldsymbol{i}}_s) + K_{res}\mathbf{R}_\theta \boldsymbol{x}_{\mathsf{dq}} \\ \frac{\mathsf{d}\boldsymbol{x}_{\mathsf{dq}}}{\mathsf{d}t} &= -K_0 \boldsymbol{x}_{\mathsf{dq}} + \mathbf{R}_\theta^\top (\boldsymbol{i}_s - \hat{\boldsymbol{i}}_s)\,. \end{aligned} \tag{28}$$

Here, K_s is the gain of the proportional term, and K_{res} is the gain of an integral term implemented in the dq-frame rotating with the eSM angle θ, while K_0 is used to limit the DC-gain of the integrator. Rotation by θ_g may also be used. Controller (28), seen in yellow in Fig. 10, is responsible solely for compensating for the internal-model error $\boldsymbol{i}_s - \hat{\boldsymbol{i}}_s$. In a parallel loop, matching-control produces the path variable $\hat{\boldsymbol{i}}_s$ and its associated feed-forward injection.

Although its purpose is to improve tracking accuracy, this controller can be shown to preserve the stability properties from Appendix B. Finally, by employing the first-order control structure (22) for the PQ-tracking case (bottom side of Fig. 10), we obtain a direct angle control method, similar in complexity to carrier-based DPC.

F. Extension to multiple circuit elements

Consider the case of an inverter with an LCL-filter, i.e. consisting of a switching-side inductor L_{s_1}, a shunt capacitor C_f and a grid-side inductor L_{s_2}. The extension of this methodology is done by including the dynamics of the filter elements and their associated internal model solutions $\hat{\boldsymbol{i}}_{s_1}$, $\hat{\boldsymbol{v}}_f$ and $\hat{\boldsymbol{i}}_{s_2}$. The synchronization potential (16) then becomes

$$\mathcal{S}(\theta_{dq}) = \tfrac{1}{2}\hat{\boldsymbol{i}}_{s_1}^\top L_{s_1} \hat{\boldsymbol{i}}_{s_1} - \tfrac{1}{2}\hat{\boldsymbol{v}}_f^\top C_f \hat{\boldsymbol{v}}_f + \tfrac{1}{2}\hat{\boldsymbol{i}}_{s_2}^\top L_{s_2} \hat{\boldsymbol{i}}_{s_2}\,. \tag{29}$$

This typically yields a similar gradient as in Fig. 7, but with the minimum shifted slightly away from zero. We also refer to [31] for the multi-machine generalization to networks with inductive edges and capacitive nodes.

IV. Regulation of a weak grid

We now turn to the second scenario. The inverter is required to regulate the AC voltage of a (local) weak bus to a given amplitude v_f^*. To include in our analysis the AC-bus dynamics, we augment (4) with a three-phase capacitor to ground, to which we attach a parallel (resistive) admittance and a sinusoidal current source modelling the presence of another converter, or a weak grid, as shown in Fig. 11; see also the equivalent circuit in Fig. 4. We have

$$\frac{\mathsf{d}\theta}{\mathsf{d}t} = \eta u_{dc} \tag{30a}$$

$$C_{dc}\frac{\mathsf{d}u_{dc}}{\mathsf{d}t} = -G_{dc}u_{dc} + i_{dc} + \mu\left[\begin{smallmatrix} -\sin\theta \\ \cos\theta \end{smallmatrix}\right]^\top \boldsymbol{i}_s \tag{30b}$$

$$L_s\frac{\mathsf{d}\boldsymbol{i}_s}{\mathsf{d}t} = -R_s\boldsymbol{i}_s + \boldsymbol{v}_f - \mu\left[\begin{smallmatrix} -\sin\theta \\ \cos\theta \end{smallmatrix}\right] u_{dc} \tag{30c}$$

$$C_f\frac{\mathsf{d}\boldsymbol{v}_f}{\mathsf{d}t} = -G_f\boldsymbol{v}_f - \boldsymbol{i}_s - \boldsymbol{i}_g\,, \tag{30d}$$

where C_f is the AC-filter capacitance, G_f represents the combined resistive losses and loads associated to the AC-bus, while the load current $\boldsymbol{i}_g$ represents a measurable vector of constant magnitude i_0, rotating at constant velocity ω_0.

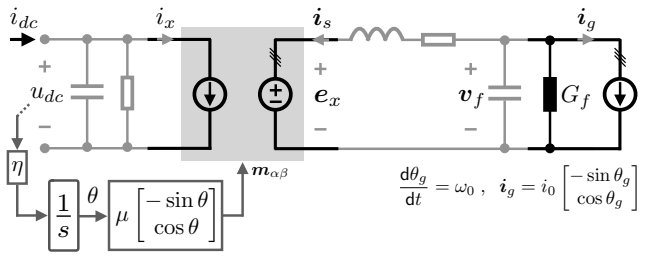

Fig. 11. Equivalent circuit of the eSM connected to a weak grid.

A. Voltage control and grid-forming behavior

Similarly to Section III-A, we start by considering a well regulated DC-bus and the sinusoidal current source $\boldsymbol{i}_g$ defined in Fig. 11. The steady-state response induced by the stiff angle dynamics is expressed in $\alpha\beta$-frame as

$$\hat{\boldsymbol{i}}_s = -(\mathbf{Y}_f^{-1} + \mathbf{Z}_s)^{-1}\big(\mu u_{dc}^* \left[\begin{smallmatrix} -\sin\theta \\ \cos\theta \end{smallmatrix}\right] + \mathbf{Y}_f^{-1}\boldsymbol{i}_g\big) \tag{31a}$$

$$\hat{\boldsymbol{v}}_f = (\mathbf{Z}_s\mathbf{Y}_f + \mathbf{I})^{-1}\big(\mu u_{dc}^* \left[\begin{smallmatrix} -\sin\theta \\ \cos\theta \end{smallmatrix}\right] - \mathbf{Z}_s\boldsymbol{i}_g\big), \tag{31b}$$

where $\mathbf{Y}_f = \left[\begin{smallmatrix} G_f & -\omega_0 C_f \\ \omega_0 C_f & G_f \end{smallmatrix}\right]$ includes the grid admittance.

In the aim of regulating the voltage magnitude $\|\boldsymbol{v}_f\|$ to the set-point v_f^*, we solve for the modulation length μ in (31b)

$$\hat{\mu}_f = \frac{\left[\begin{smallmatrix} -\sin\theta \\ \cos\theta \end{smallmatrix}\right]^\top \mathbf{Z}_s\boldsymbol{i}_g}{u_{dc}^*} + \sqrt{\left(\frac{\left[\begin{smallmatrix} -\sin\theta \\ \cos\theta \end{smallmatrix}\right]^\top \mathbf{Z}_s\boldsymbol{i}_g}{u_{dc}^*}\right)^2 + \frac{\|\mathbf{Z}_s\mathbf{Y}_f + \mathbf{I}\|^2 v_f^{*2} - \|\mathbf{Z}_s\boldsymbol{i}_g\|^2}{u_{dc}^{*2}}}$$

by taking the positive solution of the quadratic equation $\hat{\boldsymbol{v}}_f^\top\hat{\boldsymbol{v}}_f = v_f^{*2}$. This solution exists if $\|\mathbf{Z}_s\mathbf{Y}_f + \mathbf{I}\|^2 v_f^{*2} - \|\mathbf{Z}_s\boldsymbol{i}_g\|^2 > 0$ holds [22]. Compared to (25a), $\hat{\mu}_f$ also requires the eSM angle θ apart from the grid measurement $\boldsymbol{i}_g$. By choosing $\mu = \hat{\mu}_f$, we have that $\|\hat{\boldsymbol{v}}_f\| = v_f^*$ for all time and, due to the internal stability property, $\|\boldsymbol{v}_f\| \to v_f^*$ as $t \to \infty$.

In this manner, we have decoupled AC-voltage control from angle behavior, thus enabling the grid-forming operation. The DC-regulation requirement still needs to be carried out by i_{dc}, as in (22b) or via a PID design. Since the angle difference is left unregulated, the load current is able to extract an unbounded amount of active power (limited only by the DC source). In the next subsection we shall see how to control this power delivery.

B. Energy shaping and droop control

We define the active and reactive power taken by $\boldsymbol{i}_g$ as

$$\begin{aligned} P_f &= \boldsymbol{i}_g^\top \boldsymbol{v}_f \\ Q_f &= \boldsymbol{i}_g^\top \left[\begin{smallmatrix} 0 & 1 \\ -1 & 0 \end{smallmatrix}\right] \boldsymbol{v}_f \end{aligned} \quad \Big| \quad \begin{aligned} \hat{P}_f(\theta_{dq}) &= \boldsymbol{i}_g^\top \hat{\boldsymbol{v}}_f \\ \hat{Q}_f(\theta_{dq}) &= \boldsymbol{i}_g^\top \left[\begin{smallmatrix} 0 & 1 \\ -1 & 0 \end{smallmatrix}\right] \hat{\boldsymbol{v}}_f\,. \end{aligned} \tag{32}$$

Consider the scenario in which a power set-point P_f^* is given in addition to v_f^*. The control objectives become:

(*i*) DC-bus regulation: $u_{dc} \to u_{dc}^*$;
(*ii*) grid-support: $\theta_{dq} \to \theta_{dq}^*$ s.t. $\hat{P}_f(\theta_{dq}^*) = P_f^*$, $\|\hat{\boldsymbol{v}}_f\| = v_f^*$;
(*iii*) internal stability: $\boldsymbol{i}_s \to \hat{\boldsymbol{i}}_s$ and $\boldsymbol{v}_f \to \hat{\boldsymbol{v}}_f$.

By using the internal model relation (31b) in (32) and according to the steps shown in Appendix C, we obtain

$$\hat{P}_f(\theta_{dq}) - \hat{P}_f(\theta_{dq}^*) = \nabla\hat{Q}_f(\theta_{dq}) - \nabla\hat{Q}_f(\theta_{dq}^*)\,. \tag{33}$$

This identity allows us to deduce a suitable synchronization energy function, via the Bregman divergence [32] of $\hat{Q}_f$

$$\mathcal{W}(\theta_{dq}) = \tfrac{1}{\omega_0}\big(\hat{Q}_f(\theta_{dq}) - \hat{Q}_f(\theta^*_{dq}) - \nabla\hat{Q}_f(\theta^*_{dq})(\theta_{dq}-\theta^*_{dq})\big)\,,$$

seen in Fig. 12, which conveniently yields the gradient term

$$\nabla\mathcal{W}(\theta_{dq}) = \tfrac{1}{\omega_0}\big(\nabla\hat{Q}_f(\theta_{dq}) - \nabla\hat{Q}_f(\theta^*_{dq})\big). \tag{34}$$

Remark 2 (Constant μ) *In this subsection we fix $\mu^*_f = \hat{\mu}_f(\theta^*_{dq})$, given a set-point (P^*_f, v^*_f). A constant modulation length such as $\mu = \mu^*_f$ is technically required in the derivation of equation* (33)*, but can be relaxed in practice. Alternatively, we can set $\mu = \frac{1}{u^*_{dc}}\|\mathbf{Z}_s\mathbf{Y}_f+\mathbf{I}\|v^*_f$, in which case the amplitude $\|\boldsymbol{v}_f\|$ would droop with increasing load $\|\boldsymbol{i}_g\|$.*

By using (33), we recover conventional, active-power droop as the synchronizing torque

$$\tfrac{1}{u^*_{dc}}(\hat{P}_f(\theta_{dq}) - P^*_f) = \eta\nabla\mathcal{W}(\theta_{dq})\,, \tag{35}$$

and reuse the control structure (17), with $\mathcal{W}$ instead of $\mathcal{S}$

$$i_{dc} = \underbrace{-K_p(u_{dc}-u^*_{dc})}_{\text{P-control}} + \underbrace{G_{dc}u^*_{dc} + \hat{i}_x}_{\text{steady-state bias}} \underbrace{-\eta\nabla\mathcal{W}(\theta_{dq})}_{\text{synchronization}}\,. \tag{36}$$

The behavior is such that active-power droop drives θ_{dq} to the operating point where $\hat{P}_f(\theta^*_{dq}) = P^*_f$. Finally, since (36) can be used in conjunction with $\mu = \mu^*_f$, we conclude that the set-point (P^*_f, v^*_f) is achieved asymptotically as $t \to \infty$ via the energy-minimization feature of gradient descent.

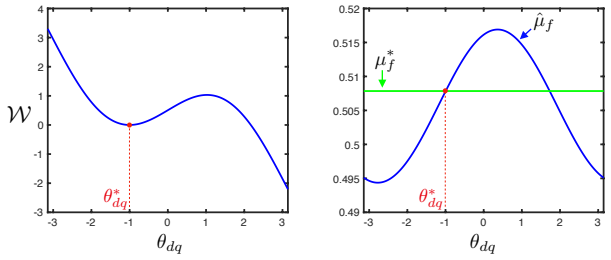

Fig. 12. The synchronization potential $\mathcal{W}$ (left) and the modulation lengths $\mu^*_f = \hat{\mu}_f(\theta^*_{dq})$ and $\hat{\mu}_f$ (right) as functions of θ_{dq} for the set-point $P^*_f = 326$W, $v^*_f = 208$V, corresponding to the minimizer $\theta^*_{dq} = -1$.

From an energy conservation perspective, if we define the steady-state AC-losses as

$$\hat{P}_{loss}(\theta_{dq}) = \tfrac{1}{2}\hat{\boldsymbol{i}}_s^\top R_s\hat{\boldsymbol{i}}_s + \tfrac{1}{2}\hat{\boldsymbol{v}}_f^\top G_f\hat{\boldsymbol{v}}_f\,, \tag{37}$$

we see that they are related to the DC-side current by

$$\hat{i}_x(\theta_{dq}) = \tfrac{1}{u^*_{dc}}(\hat{P}_{loss}(\theta_{dq}) + \hat{P}_f(\theta_{dq}))\,. \tag{38}$$

This, together with (35), allows us to reinterpret (36) as

$$i_{dc} = \underbrace{-K_p\tilde{u}_{dc}}_{\text{P-control}} + \tfrac{1}{u^*_{dc}}\underbrace{\big(G_{dc}u^{*2}_{dc} + \hat{P}_{loss}(\theta_{dq}) + P^*_f\big)}_{\text{active power injection}}\,, \tag{39}$$

which, as together with (18), suggests that, in order for large-signal synchronization to occur, the appropriate amount of active power must be injected from the DC-side.

This formulation also reveals that, in case of an overload, a saturation of i_{dc} would act as a curtailment in the effective set-point P^*_f, corresponding to a reduction in angle difference, while still allowing the grid forming operation. This particular ability of matching control has also been shown in [14] to survive large-load transients in situations where conventional cascaded-based and VSM controllers became unstable.

Remark 3 (Enabling droop control) *As in Section III-C, the synchronizing torque can drive the eSM angle directly*

$$\frac{\mathrm{d}\theta}{\mathrm{d}t} = \eta u_{dc} - \underbrace{k\big(\hat{P}_f(\theta_{dq}) - P^*_f\big)}_{k'\nabla\mathcal{W}} \tag{40}$$

where $k' = k\omega_0$ according to (35) *and k is a PLL gain. This resembles standard droop-control, the difference being that the* AC*-side frequency is replaced by the* DC*-bus measurement.*

The stability analysis in Appendix B pertains when replacing $\mathcal{S}(\theta_{dq})$ with $\mathcal{W}(\theta_{dq})$ and extending the Hamiltonian analysis to account for the capacitor dynamics. Finally, both the stiff and weak grid scenarios are compatible with the two types of energy function, $\mathcal{S}$ or $\mathcal{W}$, upon appropriate choice of modulation μ, see Table I in the Appendix for a general overview.

V. A Two-converter Micro-grid

So far we have seen two distinct behaviors, both offering the frequency support of a SM. In Section III-D a grid-following mechanism tracks a PQ set-point by assigning the modulation magnitude μ and its internal angle relative to a stiff bus. Then, in Section IV-B, a grid-forming mechanism regulates the AC-bus voltage via the modulation factor μ and, independently, the active power injection by regulating its internal angle relative to a sinusoidal disturbance. To validate experimentally the two systems, we set them up front-to-front, as seen in Fig. 13. Although both units feature an LC output filter, when shorted together, i.e. when the relays are closed, the two capacitors form a single AC-bus to be regulated by the grid-forming unit (index 1), while the grid-feeding unit (index 2) injects active and reactive power and helps supply the load.

A. Experimental setup

This experiment is performed on a general-purpose test-bench consisting of 8 IGBT half-bridges [33], passive elements, 16 analog sensors and a Central Processing Unit (CPU) provided by Imperix SA. The parameters of the two inverters are as follows: $C_{dc_{1,2}} = 1mF$, $G_{dc_{1,2}} = 9mS$, $L_{s_{1,2}} = 1.5mH$, $R_{s_{1,2}} = 1\Omega$, $C_{f_{1,2}} = 3.5\mu$ and $G_f = 15.6mS$. On the DC-side, the two busses have independent, floating grounds, while on the AC-side, the differential mode capacitors are connected in two different star-points, independent from the star-point of the resistive load.

The setup adopts the IEEE $60Hz$, $208V$ line-to-line RMS grid standard, at which the load conductance G_f draws $660W$, representing a light-load scenario. The CPU drives all PWM channels and samples all inductor currents and capacitor voltages at a frequency of $15.6kHz$, triggered at the peak of a symmetric triangular PWM carrier. The entire code, compiled from a Simulink .slx file, is executed in the same interrupt cycle for both units. All capture waveforms are signals from

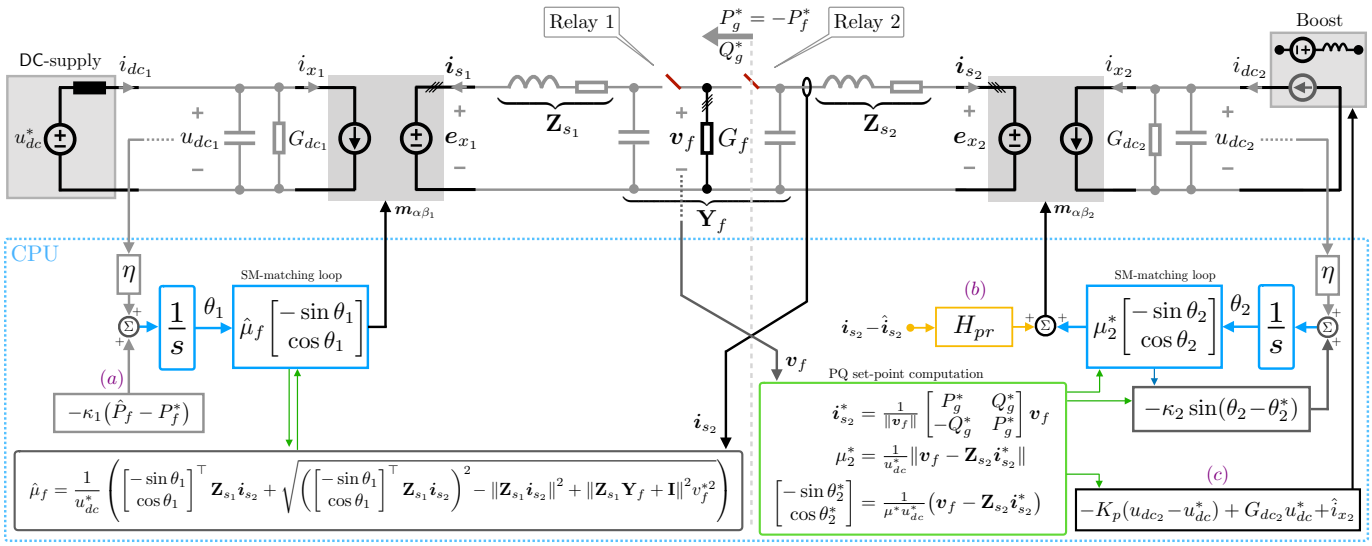

Fig. 13. Experiment implementation of the two-inverter system connected front-to-front. Index 1 denotes the grid-forming and index 2 the grid-feeding unit. Here, (a) is optional and does not affect the normal operation, (b) is used as described in Section III-E to compensate for the model inaccuracy and (c) is the control law for i_{dc_2}, implemented through a boost converter. The required internal-model variables were computed according to (41).

the CPU which are sent out, at every interrupt, via 4 digital-to-analog channels to the oscilloscope.

In Fig. 13, the source i_{dc_1} represents the current drawn from a DC lab power supply charging u_{dc_1} to $420V$. The current i_{dc_2} represents the reference given to an intermediate boost converter with the task of charging u_{dc_2} to $u^*_{dc} = 420V$ via CPU-controlled PWM. The boost converter is supplied from a second DC-power supply and is placed upstream of inverter 2 in order to freely assign the DC-bus regulation strategy. The implementation is nonetheless according to Section III-C, namely angle control is done separately from DC-bus control. This has shown better overall behavior, in particular regarding disturbance rejection.

Even though both controllers run on the same CPU, a decentralised control scheme is considered. When both relays are closed, the two AC-filter capacitors are lumped in one which, together with resistive load G_f, forms the weak grid admittance $\mathbf{Y}_f$. In terms of measurement, Unit 1 (grid-forming) has access to its own DC-link u_{dc_1}, inductor current $\boldsymbol{i}_{s_1}$ and the common AC-capacitor voltage $\boldsymbol{v}_f$ (but these latter two are not used), as well as the current drawn from the AC-bus by Unit 2 (namely $\boldsymbol{i}_{s_2}$). This is required for computing $\hat{\mu}_f$ for voltage control and $\hat{P}_f$ in the droop scheme. Unit 2 (grid-following) has access to u_{dc_2}, $\boldsymbol{i}_{s_2}$ and the AC-bus voltage it connects to, namely $\boldsymbol{v}_f$, which is required for computing μ^*_2 and θ^*_2 in the PQ-tracking scheme. The droop control (40) designed for Unit 1 was eventually not used because the angle difference is already regulated by the second converter. We have not observed any change in behavior for $\kappa_1 > 0$, while giving the same power set-point $P^*_f = -P^*_g$ to Unit 1. Throughout the experiment we fix $\kappa_1 = 0$ and $\kappa_2 = 200$. In order to track well the PQ set-point, a proportional-resonant control loop was added to Unit 2 in the form of the transfer function $H_{pr}(s)$, as per Section III-E.

Apart from the computations shown in Fig. 13, the following expressions have also been evaluated at each time step

$$\hat{P}_f = \boldsymbol{i}_{s_2}^\top (\mathbf{Z}_{s_1}\mathbf{Y}_f + \mathbf{I})^{-1}\big(\hat{\mu}_f u^*_{dc}\left[\begin{smallmatrix}-\sin\theta_1\\ \cos\theta_1\end{smallmatrix}\right] - \mathbf{Z}_{s_1}\boldsymbol{i}_{s_2}\big) \quad (41a)$$

$$\hat{\boldsymbol{i}}_{s_2} = \mathbf{Z}_{s_2}^{-1}\big(\boldsymbol{v}_f - \mu^*_2 u^*_{dc}\left[\begin{smallmatrix}-\sin\theta_2\\ \cos\theta_2\end{smallmatrix}\right]\big) \quad (41b)$$

$$\hat{i}_{x_2} = \mu^*_2 u^*_{dc}\left[\begin{smallmatrix}-\sin\theta_2\\ \cos\theta_2\end{smallmatrix}\right]^\top \mathbf{Z}_{s_2}^{-1}\big(\boldsymbol{v}_f - \mu^*_2 u^*_{dc}\left[\begin{smallmatrix}-\sin\theta_2\\ \cos\theta_2\end{smallmatrix}\right]\big) \quad (41c)$$

B. Connecting Unit 2 to Unit 1 + Load

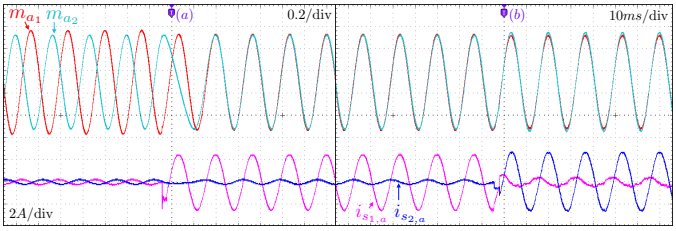

Fig. 14. Connecting G_f to the AC-bus $\boldsymbol{v}_f$ of Unit 1 via Relay 1 (a), and then connecting Unit 2 via Relay 2 (b) while tracking set-point $(P^*_g, Q^*_g) = (660, 0)$. Showing modulation, phase-a, of Unit 1 and of Unit 2, inductor current, phase-a, of Unit 1 and of Unit 2.

To observe how the two systems synchronize, consider the waveforms in Fig. 14. Initially, before trigger (a) occurs, Unit 1 is disconnected from the load and Unit 2 measures zero voltage on its capacitor since both relays are open. The two units are completely independent, and they each produce a voltage on the local LC filter (seen in the initial no-load currents). The synchronizing torque is inactive on both sides and the angle difference is unregulated. At moment (a), the load G_f is connected via Relay 1 to Unit 1, which takes over the regulation of the voltage $\boldsymbol{v}_f$. At the same time, Unit 2 senses this voltage to the left of Relay 2 and so, its synchronizing torque starts driving the angle until the two systems become in-phase. At moment (b), Relay 2 is closed

and Unit 2 safely connects to the AC-bus controlled by Unit 1 and starts tracking its given PQ set-point by adjusting its magnitude and angle.

C. Tracking a step in P_g^* and in Q_g^*

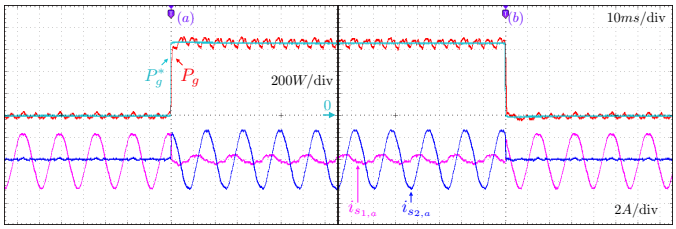

Fig. 15. Both relays remain closed while the set-point P_g^* for Unit 2 goes from 0 to $660W$ at trigger (a) and then back to 0 at (b); $Q_g^* = 0$. Showing P_g^*, P_g, inductor current, phase-a, of Unit 1 and of Unit 2.

Fig. 15 shows the transient in active power delivered by Unit 2. We observed good PQ set-point tracking performance when the internal-model compensation was added to $\boldsymbol{m}_{\alpha\beta_2}$.

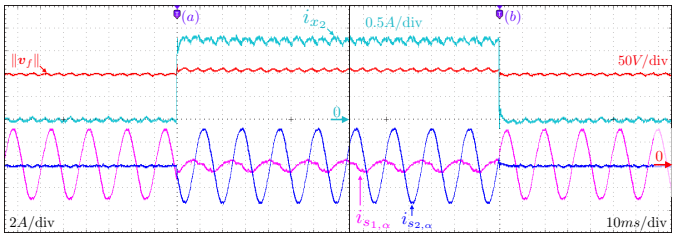

Fig. 16. Idem Fig. 15, P_g^* from 0 to $660W$ (a) to 0 (b); $Q_g^* = 0$. Showing $\|\boldsymbol{v}_f\|$, i_{x_2}, inductor current, phase-alpha, of Unit 1 and of Unit 2.

Fig. 16 shows the same transient in active power as in Fig. 15 but with different probed signals. Notice the step in DC-side current i_{x_2} indicating the fast jump in power. Further observe the performance of the voltage control showing about 3% droop from full load to no load. This is mainly due to the parameter uncertainty affecting the computation of $\hat{\mu}_f$.

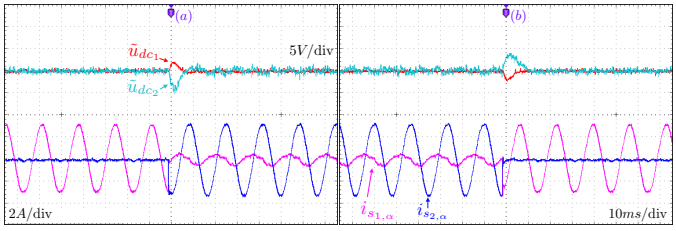

Fig. 17. Idem Fig. 15, P_g^* from 0 to $660W$ (a) to 0 (b); $Q_g^* = 0$. Showing $\tilde{u}_{dc_1}$, $\tilde{u}_{dc_2}$, inductor current, phase-alpha, of Unit 1 and of Unit 2.

Fig. 17 shows the same transient in active power as in Fig. 15 but with different probed signals. Notice the well regulated DC-busses, Unit 1 showing less noise and a faster transient since it is connected directly to a lab power supply.

Fig. 18 shows the set-point change in reactive power delivered by Unit 2 with similar, but of slightly slower, tracking performance as the one for active power. Due to common-mode noise affecting our measurements, we were not able to completely eliminate low-order harmonics, most prominently seen here.

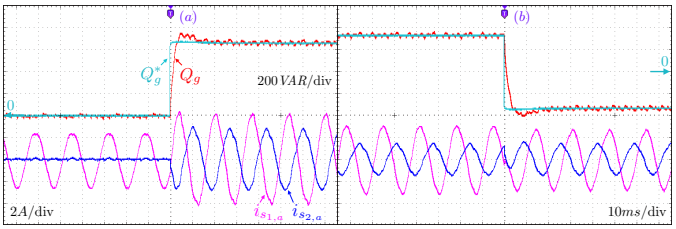

Fig. 18. Both units are connected to the load while the set-point Q_g^* goes from 0 to $660VAR$ at trigger (a) and then from $330VAR$ to $-330VAR$ at trigger (b); $P_g^* = 0$. Showing Q_g^*, Q_g, inductor current, phase-a, of Unit 1 and of Unit 2.

D. Tracking the internal model

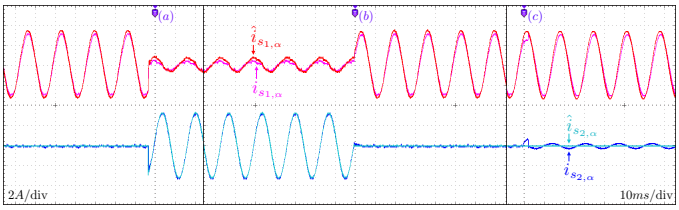

Fig. 19. Both relays are initially closed while set-point P_g^* goes from 0 to $660W$ (a) and back to 0 (b). Then Unit 2 is disconnected via Relay 2 at trigger (c); $Q_g^* = 0$. Showing $i_{s_{1,\alpha}}$, $\hat{i}_{s_{1,\alpha}}$, $i_{s_{2,\alpha}}$ and $\hat{i}_{s_{2,\alpha}}$.

Fig. 19 shows the same step changes in P_g^* from 0 to full load and back to 0 as before, after which Unit 2 is disconnected via Relay 2 at trigger (c). We see that the path-following objective (*iii*) is affected by external factors, particularly in Unit 1 which does not use active internal-model compensation.

VI. Conclusion

This paper is based on the following idea: instead of taking the DC-bus as a voltage source, we consider its (nonlinear) dynamics and treat the whole converter as a modulated energy transfer device, i.e. a gyrator. This crucial step has revealed:

- the inherent synchronization torque is the gradient of the energy function anticipating the inductor storage;
- the large-signal transient behavior is similar to that of a damped pendulum under gravity;
- the DC-bus based PLL can allow seamless transition from grid-following to grid-forming, with potential applications to islanded and black-start operations;
- inertia and damping can be augmented by the DC-side current injection implementing PD-control;
- by injecting just the right amount of instantaneous power from the DC-side, droop control emerges;
- steady-state power-flow control can deferred to the saturation of the DC-side current.

In more detail, we have seen that, by augmenting a DC-bus integrator, we are able to exactly match the SM dynamics and produce unhampered power flow from AC to DC, merging the benefits of the electrical machine and inverter. Subsequently, we have identified a canonical control structure allowing us, on the one hand, to replace the conventional PLL with the gradient of a synchronization energy acting on the converter angle. On the other hand, this potential energy can be reshaped

as energy of reactive-kind, the gradient of which yields active-power droop, seen as another synchronization torque.

APPENDIX A
SYNCHRONOUS MACHINE MODEL

Consider a non-salient rotor, single-pole pair, DC-excited SM without damper windings [34], written in $\alpha\beta$-frame as

$$\frac{\mathsf{d}\theta}{\mathsf{d}t} = \omega \tag{42a}$$
$$M\frac{\mathsf{d}\omega}{\mathsf{d}t} = -D\omega - \tau_e + \tau_m \tag{42b}$$
$$\frac{\mathsf{d}\lambda_r}{\mathsf{d}t} = -R_r i_r + u_r \tag{42c}$$
$$\frac{\mathsf{d}\boldsymbol{\lambda}_s}{\mathsf{d}t} = -R_s \boldsymbol{i}_s + \boldsymbol{v}_g\,. \tag{42d}$$

Here M and D are the rotor moment of inertia and damping coefficient, θ is the rotor angle, and ω its angular velocity. We assume that the rotor is driven by the mechanical torque τ_m and has its terminals connected to a grid voltage $\boldsymbol{v}_g$, as does the inverter. We further denote τ_e as the air-gap torque, λ_r as the rotor flux linkage (scalar), i_r its current and u_r the voltage applied to the rotor terminals. Moreover, $\boldsymbol{\lambda}_s$ denotes the stator flux linkage (vector) and $\boldsymbol{i}_s$ its current. The losses in the rotor and stator are represented respectively by R_r and R_s.

We consider the electromagnetic energy stored in the SM

$$W_e = \tfrac{1}{2}\begin{bmatrix}\lambda_{s_\alpha}\\ \lambda_{s_\beta}\\ \lambda_r\end{bmatrix}^\top \begin{bmatrix} L_s & 0 & L_m\cos\theta \\ 0 & L_s & L_m\sin\theta \\ L_m\cos\theta & L_m\sin\theta & L_r\end{bmatrix}^{-1}\begin{bmatrix}\lambda_{s_\alpha}\\ \lambda_{s_\beta}\\ \lambda_r\end{bmatrix}, \tag{43}$$

where L_s and L_r are the stator and rotor self-inductances, respectively, and L_m is the mutual inductance of the machine. Accordingly, the electrical quantities are related as

$$\tau_e = \tfrac{\partial W_e}{\partial\theta} = -L_m i_r \begin{bmatrix}-\sin\theta\\ \cos\theta\end{bmatrix}^\top \boldsymbol{i}_s \tag{44a}$$
$$i_r = \tfrac{\partial W_e}{\partial\lambda_r} \;\Leftrightarrow\; \lambda_r = L_r i_r + L_m\begin{bmatrix}\cos\theta\\ \sin\theta\end{bmatrix}^\top \boldsymbol{i}_s \tag{44b}$$
$$\boldsymbol{i}_s^\top = \tfrac{\partial W_e}{\partial\boldsymbol{\lambda}_s} \;\Leftrightarrow\; \boldsymbol{\lambda}_s = L_s\boldsymbol{i}_s + L_m\begin{bmatrix}\cos\theta\\ \sin\theta\end{bmatrix} i_r \tag{44c}$$

Using Faraday's law, we define the rotor and stator electromotive forces as $e_r = \frac{\mathsf{d}}{\mathsf{d}t}(\lambda_r - L_r i_r)$ and, respectively, $\boldsymbol{e}_s = \frac{\mathsf{d}}{\mathsf{d}t}(\boldsymbol{\lambda}_s - L_s\boldsymbol{i}_s)$, which we expand below

$$\boldsymbol{e}_s = L_m i_r\begin{bmatrix}-\sin\theta\\ \cos\theta\end{bmatrix}\omega + L_m\tfrac{\mathsf{d}i_r}{\mathsf{d}t}\begin{bmatrix}\cos\theta\\ \sin\theta\end{bmatrix}. \tag{45}$$

Suppose now that the rotor current is regulated to a constant i_r^* via a control such as $u_r = R_r i_r^* + e_r$. As a consequence, when $i_r = i_r^*$, equation (42c) becomes $L_r\frac{\mathsf{d}i_r}{\mathsf{d}t} = 0$, so it can be set aside. The system reduces to (7).

APPENDIX B
ENERGY-BASED STABILIZATION OF THE ESM

Consider the eSM (11), in the stiff grid scenario of Section III-A and written in coordinates θ_{dq}, $\tilde{u}_{dc}$, $\tilde{\boldsymbol{i}}_{dq} = \boldsymbol{i}_{dq} - \hat{\boldsymbol{i}}_{dq}$ and with the input transformation $\tilde{i}_{dc} = i_{dc} - G_{dc}u_{dc}^*$,

$$\frac{\mathsf{d}\theta_{dq}}{\mathsf{d}t} = \eta\tilde{u}_{dc} \tag{46a}$$
$$C_{dc}\frac{\mathsf{d}\tilde{u}_{dc}}{\mathsf{d}t} = -G_{dc}\tilde{u}_{dc} + \tilde{i}_{dc} - \hat{i}_x + \mu\begin{bmatrix}-\sin\theta_{dq}\\ \cos\theta_{dq}\end{bmatrix}^\top\tilde{\boldsymbol{i}}_{dq} \tag{46b}$$
$$L_s\frac{\mathsf{d}\tilde{\boldsymbol{i}}_{dq}}{\mathsf{d}t} = -\mathbf{Z}_s\tilde{\boldsymbol{i}}_{dq} - R_s\mathbf{Z}_s^{-1}\mu\begin{bmatrix}-\sin\theta_{dq}\\ \cos\theta_{dq}\end{bmatrix}\tilde{u}_{dc}\,. \tag{46c}$$

Consider again the energy function (21), accounting for the deviation from the origin of the transient system (46), as

$$\tilde{\mathcal{H}}(\theta_{dq},\tilde{u}_{dc},\tilde{\boldsymbol{i}}_{dq}) = \tfrac{1}{2}C_{dc}\tilde{u}_{dc}^2 + \tfrac{1}{2}\tilde{\boldsymbol{i}}_{dq}^\top L_s\tilde{\boldsymbol{i}}_{dq} + \mathcal{S}(\theta_{dq})\,.$$

In the spirit of passivity-based control, input (17) is chosen such that it renders $\tilde{\mathcal{H}}$ decreasing along the error trajectories:

$$\frac{\mathsf{d}\tilde{\mathcal{H}}}{\mathsf{d}t} = -(G_{dc}+K_p)\tilde{u}_{dc}^2 - \tilde{\boldsymbol{i}}_{dq}^\top R_s\tilde{\boldsymbol{i}}_{dq} - \tilde{\boldsymbol{i}}_{dq}^\top T(\theta_{dq})\tilde{u}_{dc}\,,$$

where $T(\theta_{dq}) = \mu\omega_0 L_s\mathbf{Z}_s^{-1}\begin{bmatrix}\cos\theta_{dq}\\ \sin\theta_{dq}\end{bmatrix}$. To guarantee that $\frac{\mathsf{d}\tilde{\mathcal{H}}}{\mathsf{d}t}$ is negative definite in $(\tilde{u}_{dc},\tilde{\boldsymbol{i}}_{dq})$, it is sufficient to assign K_p such that $\frac{G_{dc}+K_p}{\eta^2} > \frac{L_s^2}{4R_s}\frac{\mu^2u_{dc}^{*2}}{\|\mathbf{Z}_s\|^2}$. This, together with boundedness of the angle, sets up the conditions to apply the LaSalle invariance principle and conclude that all trajectories $(\theta_{dq},\tilde{u}_{dc},\tilde{\boldsymbol{i}}_{dq})$ of the transient system (46) globally converge to the set of points where $\tilde{u}_{dc} = 0$, $\nabla\mathcal{S}(\theta_{dq}) = 0$, and $\tilde{\boldsymbol{i}}_{dq} = 0$, thus achieving the intended objectives (*i*), (*ii*) and (*iii*), respectively. Furthermore, some degree of robustness is induced from the passivity property of the closed loop.

APPENDIX C
DERIVATION OF THE REACTIVE POWER GRADIENT

We define $\boldsymbol{i}_{g_{dq}} = \mathbf{R}_{\theta_g}^\top\boldsymbol{i}_g$ and consider (31b) in (32) in grid-attached dq-frame with modulation length $\mu = \mu_f^*$

$$\begin{aligned}
&\hat{P}_f(\theta_{dq}) - \hat{P}_f(\theta_{dq}^*) = \\
&= \boldsymbol{i}_{g_{dq}}^\top(\mathbf{Z}_s\mathbf{Y}_f + \mathbf{I})^{-1}\left(\mu u_{dc}^*\begin{bmatrix}-\sin\theta_{dq}\\ \cos\theta_{dq}\end{bmatrix} - \mathbf{Z}_s\boldsymbol{i}_{g_{dq}}\right)\\
&- \boldsymbol{i}_{g_{dq}}^\top(\mathbf{Z}_s\mathbf{Y}_f + \mathbf{I})^{-1}\left(\mu u_{dc}^*\begin{bmatrix}-\sin\theta_{dq}^*\\ \cos\theta_{dq}^*\end{bmatrix} - \mathbf{Z}_s\boldsymbol{i}_{g_{dq}}\right)\\
&= \boldsymbol{i}_{g_{dq}}^\top(\mathbf{Z}_s\mathbf{Y}_f + \mathbf{I})^{-1}\begin{bmatrix}0 & 1\\ -1 & 0\end{bmatrix}\left(-\mu u_{dc}^*\begin{bmatrix}\cos\theta_{dq}\\ \sin\theta_{dq}\end{bmatrix} + \mu u_{dc}^*\begin{bmatrix}\cos\theta_{dq}^*\\ \sin\theta_{dq}^*\end{bmatrix}\right)\\
&= \boldsymbol{i}_{g_{dq}}^\top\begin{bmatrix}0 & 1\\ -1 & 0\end{bmatrix}(\mathbf{Z}_s\mathbf{Y}_f + \mathbf{I})^{-1}\left(-\mu u_{dc}^*\begin{bmatrix}\cos\theta_{dq}\\ \sin\theta_{dq}\end{bmatrix} + \mu u_{dc}^*\begin{bmatrix}\cos\theta_{dq}^*\\ \sin\theta_{dq}^*\end{bmatrix}\right)\\
&= \nabla\hat{Q}_f(\theta_{dq}) - \nabla\hat{Q}_f(\theta_{dq}^*)\,.
\end{aligned}$$

The same relationship can also be derived for $\hat{P}_g$ and $\nabla\hat{Q}_g$ from (13), (23) in the stiff-grid scenario.

REFERENCES

[1] J. I. Leon, S. Kouro, L. G. Franquelo, J. Rodriguez, and B. Wu, "The essential role and the continuous evolution of modulation techniques for voltage-source inverters in the past, present, and future power electronics," *IEEE Transactions on Industrial Electronics*, vol. 63, no. 5, pp. 2688–2701, 2016.

[2] J. Rocabert, A. Luna, F. Blaabjerg, and P. Rodriguez, "Control of power converters in ac microgrids," *IEEE Transactions on Power Electronics*, vol. 27, no. 11, pp. 4734–4749, 2012.

[3] F. Blaabjerg, R. Teodorescu, M. Liserre, and A. Timbus, "Overview of control and grid synchronization for distributed power generation systems," *IEEE Transactions on Industrial Electronics*, vol. 53, no. 5, pp. 1398–1409, 2006.

[4] M. G. Taul, X. Wang, P. Davari, and F. Blaabjerg, "An overview of assessment methods for synchronization stability of grid-connected converters under severe symmetrical grid faults," *IEEE Transactions on Power Electronics*, 2019.

[5] M. Malinowski, M. Kazmierkowski, S. Hansen, F. Blaabjerg, and G. Marques, "Virtual-flux-based direct power control of three-phase pwm rectifiers," *IEEE Transactions on Industry Applications*, vol. 37, no. 4, pp. 1019–1027, 2001.

Function	(I) Stiff grid: VSC-L connected to $\boldsymbol{v}_g$ *set-points* $[a]$ (P_g^*, Q_g^*), $[b]$ i_s^* *or* $[c]$ (P_g^*, i_s^*)	(II) Weak grid: VSC-LC connected to $\boldsymbol{i}_g$ *set-points* $[a]$ (P_f^*, Q_f^*), $[b]$ v_f^* *or* $[c]$ (P_f^*, v_f^*)
$[a]$ PQ tracking $\boldsymbol{i}_s \to \hat{\boldsymbol{i}}_s \to \boldsymbol{i}_s^*$ (I) $\boldsymbol{v}_f \to \hat{\boldsymbol{v}}_f \to \boldsymbol{v}_f^*$ (II) (grid-following)	$\boldsymbol{i}_s^* = \frac{1}{\|\boldsymbol{v}_g\|^2}\begin{bmatrix} P_g^* & Q_g^* \\ -Q_g^* & P_g^* \end{bmatrix}\boldsymbol{v}_g$ $\mu^* = \frac{1}{u_{dc}^*}\|\boldsymbol{v}_g - \mathbf{Z}_s \boldsymbol{i}_s^*\|$ $\begin{bmatrix} -\sin\theta^* \\ \cos\theta^* \end{bmatrix} = \frac{1}{\mu^* u_{dc}^*}\left(\boldsymbol{v}_g - \mathbf{Z}_s \boldsymbol{i}_s^*\right)$ $\mathcal{S} = \frac{1}{2}\hat{\boldsymbol{i}}_s^\top L_s \hat{\boldsymbol{i}}_s$ $\tau_{\text{sync}} = -\nabla\mathcal{S}(\theta - \theta^*)$	$\boldsymbol{v}_f^* = \frac{1}{\|\boldsymbol{i}_g\|^2}\begin{bmatrix} P_f^* & Q_f^* \\ -Q_f^* & P_f^* \end{bmatrix}\boldsymbol{i}_g$ $\mu^* = \frac{1}{u_{dc}^*}\|(\mathbf{Z}_s\mathbf{Y}_f + \mathbf{I})\boldsymbol{v}_f^* + \mathbf{Z}_s \boldsymbol{i}_g\|$ $\begin{bmatrix} -\sin\theta^* \\ \cos\theta^* \end{bmatrix} = \frac{1}{\mu^* u_{dc}^*}\left((\mathbf{Z}_s\mathbf{Y}_f + \mathbf{I})\boldsymbol{v}_f^* + \mathbf{Z}_s \boldsymbol{i}_g\right)$ $\mathcal{S} = \frac{1}{2}\hat{\boldsymbol{i}}_s^\top L_s \hat{\boldsymbol{i}}_s - \frac{1}{2}\hat{\boldsymbol{v}}_f^\top C_f \hat{\boldsymbol{v}}_f$ $\tau_{\text{sync}} = -\nabla\mathcal{S}(\theta - \theta^*)$
$[b]$ Single AC-objective $\|\boldsymbol{i}_s\| \to \|\hat{\boldsymbol{i}}_s\| = i_s^*$ (I) $\|\boldsymbol{v}_f\| \to \|\hat{\boldsymbol{v}}_f\| = v_f^*$ (II) (grid-forming)	$\hat{\mu}_s = \frac{\begin{bmatrix} -\sin\theta \\ \cos\theta \end{bmatrix}^\top \boldsymbol{v}_g}{u_{dc}^*} + \sqrt{\left(\frac{\begin{bmatrix} -\sin\theta \\ \cos\theta \end{bmatrix}^\top \boldsymbol{v}_g}{u_{dc}^*}\right)^2 - \frac{\|\boldsymbol{v}_g\|^2 - \|\mathbf{Z}_s\|^2 i_s^{*2}}{u_{dc}^{*2}}}$	$\hat{\mu}_f = \frac{\begin{bmatrix} -\sin\theta \\ \cos\theta \end{bmatrix}^\top \mathbf{Z}_s \boldsymbol{i}_g}{u_{dc}^*} + \sqrt{\left(\frac{\begin{bmatrix} -\sin\theta \\ \cos\theta \end{bmatrix}^\top \mathbf{Z}_s \boldsymbol{i}_g}{u_{dc}^*}\right)^2 - \frac{\|\mathbf{Z}_s \boldsymbol{i}_g\|^2 - \|\mathbf{Z}_s\mathbf{Y}_f + \mathbf{I}\|^2 v_f^{*2}}{u_{dc}^{*2}}}$
$[c]$ Droop-based (grid-supporting)	$\mu = \frac{e_0}{u_{dc}^*}$ *or* $\mu = \hat{\mu}_s(\theta_{dq}^*)$ $\mathcal{W}(\theta_{dq}) = \frac{1}{\omega_0}\left(\hat{Q}_g(\theta_{dq}) - \hat{Q}_g(\theta_{dq}^*) - \nabla\hat{Q}_g(\theta_{dq}^*)(\theta_{dq} - \theta_{dq}^*)\right)$ $\tau_{\text{sync}} = -\nabla\mathcal{W}(\theta_{dq}) = -\frac{1}{\omega_0}(\hat{P}_g(\theta_{dq}) - P_g^*)$	$\mu = \frac{\|\mathbf{Z}_s\mathbf{Y}_f + \mathbf{I}\| v_f^*}{u_{dc}^*}$ *or* $\mu = \hat{\mu}_f(\theta_{dq}^*)$ $\mathcal{W}(\theta_{dq}) = \frac{1}{\omega_0}\left(\hat{Q}_f(\theta_{dq}) - \hat{Q}_f(\theta_{dq}^*) - \nabla\hat{Q}_f(\theta_{dq}^*)(\theta_{dq} - \theta_{dq}^*)\right)$ $\tau_{\text{sync}} = -\nabla\mathcal{W}(\theta_{dq}) = -\frac{1}{\omega_0}(\hat{P}_f(\theta_{dq}) - P_f^*)$

TABLE I
AN OVERVIEW OF THE CONTROLLERS FOR SOME POSSIBLE GRID-CONNECTED SCENARIOS.

[6] Y. Gui, X. Wang, and F. Blaabjerg, "Vector current control derived from direct power control for grid-connected inverters," *IEEE Transactions on Power Electronics*, 2018.

[7] F. Milano, F. Dörfler, G. Hug, D. J. Hill, and G. Verbič, "Foundations and challenges of low-inertia systems," in *2018 Power Systems Computation Conference (PSCC)*. IEEE, 2018, pp. 1–25.

[8] L. Huang, H. Xin, and Z. Wang, "Damping low-frequency oscillations through vsc-hvdc stations operated as virtual synchronous machines," *IEEE Transactions on Power Electronics*, pp. 1–1, 2018.

[9] S. D'Arco and J. A. Suul, "Virtual synchronous machines-classification of implementations and analysis of equivalence to droop controllers for microgrids," in *2013 IEEE Grenoble Conference*. IEEE, 2013, pp. 1–7.

[10] H. Bevrani, T. Ise, and Y. Miura, "Virtual synchronous generators: A survey and new perspectives," *International Journal of Electrical Power & Energy Systems*, vol. 54, pp. 244–254, 2014.

[11] L. Xiong, F. Zhuo, F. Wang, X. Liu, Y. Chen, M. Zhu, and H. Yi, "Static synchronous generator model: a new perspective to investigate dynamic characteristics and stability issues of grid-tied pwm inverter," *IEEE Transactions on Power Electronics*, vol. 31, no. 9, pp. 6264–6280, 2016.

[12] B. Wen, D. Boroyevich, R. Burgos, P. Mattavelli, and Z. Shen, "Analysis of dq small-signal impedance of grid-tied inverters," *IEEE Transactions on Power Electronics*, vol. 31, no. 1, pp. 675–687, 2016.

[13] X. Wang, L. Harnefors, and F. Blaabjerg, "Unified impedance model of grid-connected voltage-source converters," *IEEE Transactions on Power Electronics*, vol. 33, no. 2, pp. 1775–1787, 2018.

[14] A. Tayyebi, D. Groß, A. Anta, F. Kupzog, and F. Dörfler, "Interactions of grid-forming power converters and synchronous machines–a comparative study," *arXiv preprint arXiv:1902.10750*, 2019.

[15] C. Zhang, M. Molinas, X. Cai, and A. Rygg, "Understanding the nonlinear behavior and frequency stability of a grid-synchronized vsc under grid voltage dips," *arXiv preprint arXiv:1806.11529*, 2018.

[16] R. Ortega, A. Van Der Schaft, F. Castanos, and A. Astolfi, "Control by interconnection and standard passivity-based control of port-hamiltonian systems," *IEEE Transactions on Automatic control*, vol. 53, no. 11, pp. 2527–2542, 2008.

[17] A. Aguiar, J. Hespanha, and P. Kokotovic, "Path-following for nonminimum phase systems removes performance limitations," *IEEE Transactions on Automatic Control*, vol. 50, no. 2, pp. 234–239, 2005.

[18] C. Byrnes and A. Isidori, "Output regulation for nonlinear systems: an overview," *International Journal of Robust and Nonlinear Control: IFAC-Affiliated Journal*, vol. 10, no. 5, pp. 323–337, 2000.

[19] I. Cvetkovic, D. Boroyevich, R. Burgos, C. Li, M. Jaksic, and P. Mattavelli, "Modeling of a virtual synchronous machine-based grid-interface converter for renewable energy systems integration," in *2014 IEEE 15th Workshop on Control and Modeling for Power Electronics (COMPEL)*. IEEE, 2014, pp. 1–7.

[20] I. Cvetkovic, D. Boroyevich, R. Burgos, C. Li, and P. Mattavelli, "Modeling and control of grid-connected voltage-source converters emulating isotropic and anisotropic synchronous machines," in *2015 IEEE 16th Workshop on Control and Modeling for Power Electronics (COMPEL)*. IEEE, 2015, pp. 1–5.

[21] T. Jouini, C. Arghir, and F. Dörfler, "Grid-friendly matching of synchronous machines by tapping into the dc storage," *IFAC-PapersOnLine*, vol. 49, no. 22, pp. 192–197, 2016.

[22] C. Arghir, T. Jouini, and F. Dörfler, "Grid-forming control for power converters based on matching of synchronous machines," *Automatica*, vol. 95, pp. 273–282, 2018.

[23] C. Li, I. Cvetkovic, R. Burgos, and D. Boroyevich, "Assessment of virtual synchronous machine based control in grid-tied power converters," in *2018 International Power Electronics Conference (IPEC-Niigata 2018 -ECCE Asia)*, May 2018, pp. 790–794.

[24] L. Huang, H. Xin, Z. Wang, K. Wu, H. Wang, J. Hu, and C. Lu, "A virtual synchronous control for voltage-source converters utilizing dynamics of dc-link capacitor to realize self-synchronization," *IEEE Journal of Emerging and Selected Topics in Power Electronics*, vol. 5, no. 4, pp. 1565–1577, 2017.

[25] S. Curi, D. Groß, and F. Dörfler, "Control of low-inertia power grids: A model reduction approach," in *2017 IEEE 56th Annual Conference on Decision and Control (CDC)*. IEEE, 2017, pp. 5708–5713.

[26] T. Noguchi, H. Tomiki, S. Kondo, and I. Takahashi, "Direct power control of pwm converter without power source voltage sensors," in *IAS'96. Conference Record of the 1996 IEEE Industry Applications Conference Thirty-First IAS Annual Meeting*, vol. 2. IEEE, 1996, pp. 941–946.

[27] G. Escobar, A. M. Stankovic, J. M. Carrasco, E. Galván, and R. Ortega, "Analysis and design of direct power control (dpc) for a three phase synchronous rectifier via output regulation subspaces," *IEEE Transactions on Power Electronics*, vol. 18, no. 3, pp. 823–830, 2003.

[28] A. Rantzer, "Almost global stability of phase-locked loops," in *Proceedings of the 40th IEEE Conference on Decision and Control (Cat. No. 01CH37228)*, vol. 1. IEEE, 2001, pp. 899–900.

[29] B. A. Francis and W. M. Wonham, "The internal model principle of control theory," *Automatica*, vol. 12, no. 5, pp. 457–465, 1976.

[30] F. Dorfler and F. Bullo, "Synchronization and transient stability in power networks and nonuniform kuramoto oscillators," *SIAM Journal on Control and Optimization*, vol. 50, no. 3, pp. 1616–1642, 2012.

[31] C. Arghir and F. Dörfler, "Energy-based stabilization of network flows in multi-machine power systems," in *Proceedings of the 23rd International Symposium on Mathematical Theory of Networks and Systems*, 2018.

[32] C. De Persis and N. Monshizadeh, "Bregman storage functions for microgrid control," *IEEE Transactions on Automatic Control*, vol. 63, no. 1, pp. 53–68, 2018.

[33] Imperix, *PEB8032*, https://imperix.ch/products/power/peb.

[34] J. Machowski, J. Bialek, and J. Bumby, *Power system dynamics: stability and control*. John Wiley & Sons, 2011.